Volume 8
Number 23
7 December 2020
Pages 6417-6800

Biomaterials Science

rsc.li/biomaterials-science

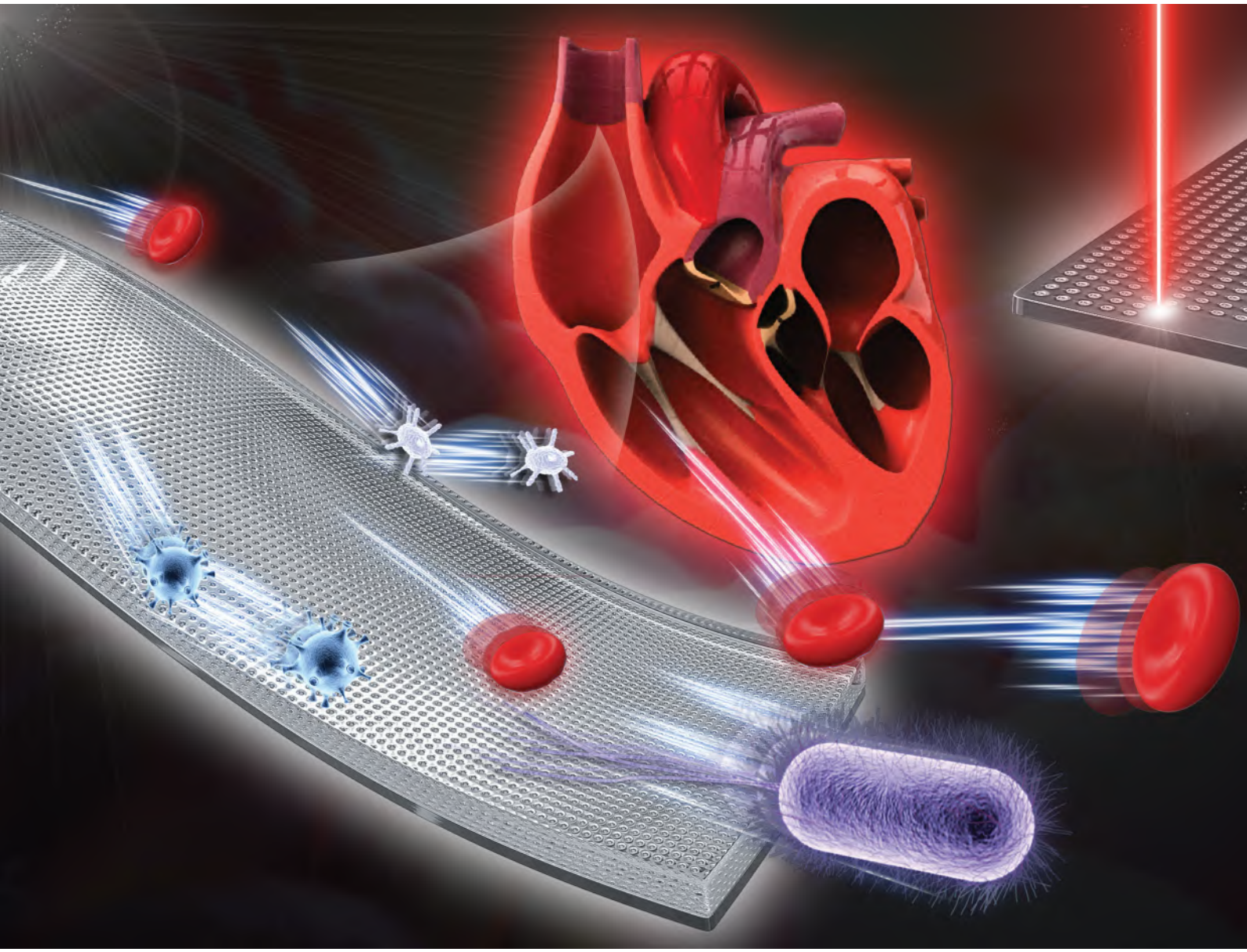

ISSN 2047-4849

ROYAL SOCIETY OF CHEMISTRY

PAPER

Qing Yang, Jiale Yong, Feng Chen *et al.*
A femtosecond Bessel laser for preparing a nontoxic slippery liquid-infused porous surface (SLIPS) for improving the hemocompatibility of NiTi alloys

European Society for Biomaterials

Biomaterials Science

ROYAL SOCIETY OF CHEMISTRY

PAPER

View Article Online
View Journal | View Issue

Cite this: *Biomater. Sci.*, 2020, **8**, 6505

A femtosecond Bessel laser for preparing a nontoxic slippery liquid-infused porous surface (SLIPS) for improving the hemocompatibility of NiTi alloys†

Yang Cheng,[a,b] Qing Yang,*[a,b] Yu Lu,[c,b] Jiale Yong,*[c,b] Yao Fang,[c,b] Xun Hou[c] and Feng Chen *[c,b]

Received 15th August 2020,
Accepted 23rd September 2020

DOI: 10.1039/d0bm01369b

rsc.li/biomaterials-science

A slippery liquid-infused porous surface (SLIPS) is able to improve the hemocompatibility of implantable medical materials, which have saved countless lives. However, the preparation of a SLIPS on an implantable metal substrate (especially NiTi alloys) is still a substantial challenge because of the great difficulty of forming abundant porous microstructures on hard metals. In this paper, a novel strategy to prepare a SLIPS on a NiTi alloy substrate is reported. We used the laser pulse train of a femtosecond Bessel laser rather than the common Gaussian beam to directly create deep porous microstructures on the surface of the implantable NiTi alloy. Based on the laser-induced porous microstructure, the SLIPS was obtained by lowering the surface energy and infusing the lubricant liquid into the pores. The as-prepared SLIPS very effectively repelled water and blood. The hemocompatibility of the NiTi alloy was greatly improved after the formation of the SLIPS by the femtosecond Bessel laser processing. It was demonstrated that the SLIPS gives the NiTi alloy a remarkable anticoagulation property, very low hemolysis rate, and antibacterial property. We believe that the laser-induced SLIPS will accelerate the broad application of metal implants in the medical field in a healthier and safer way.

1. Introduction

Medical implants (artificial heart valves, stents, vascular grafts, *etc.*) and blood-containing devices (left ventricular assist devices, heart-lung machines, *etc.*) save countless lives and play an important role in the modern medical field.[1–3] However, almost all implantable medical materials face the hemocompatibility problem caused by the blood–implant interaction.[4] The presence of implantable materials in the body will result in a multitude of side effects and even the failure of the related therapeutic procedures once coagulation, hemolysis, or infection occurs.[5] Generally, anticoagulant drugs are used to improve the hemocompatibility of implantable materials and prevent those side effects.[6,7] However, the long-term use of anticoagulant drugs not only produces additional economic and psychological stress in patients but also threatens patients' health. Effectively improving the hemocompatibility of implantable materials is still a thorny problem in medicine.

Inspired by the pitcher plant, Aizenberg *et al.* first proposed a method to prepare a slippery liquid-infused porous surface (SLIPS) that strongly repels various liquids, including blood.[8] The SLIPS was fabricated through the creation of porous microstructures, low-surface-energy modification, and the infusion of the lubricant liquid.[9–11] A liquid lubricating layer forms on the SLIPS as the lubricant is infused into the porous microstructure; thereby, a proper porous microstructure is the key to prepare the SLIPS. The stable liquid repellency and excellent anti-bioadhesion property enable the artificial SLIPS to have great potential for application in improving the hemocompatibility of the medical materials.[12–17] Leslie *et al.* demonstrated the capabilities of preventing the attachment of fibrinogen, reducing the adhesion and activation of platelets, and inhibiting thrombosis and biofouling for a SLIPS that was prepared by covalently bonding flexible perfluorocarbon molecules to a substrate.[12] Luan *et al.* wrinkled the surface of a photografting-polymerization polymer by an osmotically driven wrinkling method and further infused a fluorocarbon

[a]*School of Mechanical Engineering, Xi'an Jiaotong University, Xi'an, 710049, PR China. E-mail: yangqing@mail.xjtu.edu.cn*
[b]*The International Joint Research Laboratory for Micro/Nano Manufacturing and Measurement Technologies, Xi'an Jiaotong University, Xi'an, 710049, PR China. E-mail: chenfeng@mail.xjtu.edu.cn, jlyong@xjtu.edu.cn*
[c]*State Key Laboratory for Manufacturing System Engineering and Shaanxi Key Laboratory of Photonics Technology for Information, School of Electronic Science and Engineering, Xi'an Jiaotong University, Xi'an, 710049, PR China*

†Electronic supplementary information (ESI) available. See DOI: 10.1039/d0bm01369b

liquid into the wrinkled structure. The resultant lubricant-infused wrinkled surface prevented the formation of thrombi and avoided infection.[15] Didar *et al.* obtained a SLIPS by infiltrating a biocompatible fluorocarbon-based lubricant into fluorosilane molecules. The as-prepared SLIPS hindered the nonspecific adhesion of biomolecules and cells in blood.[17] Although an artificial SLIPS has already been proven to have high significance in medicine, the achievement of a SLIPS on medical metal substrates (especially NiTi alloys) has rarely been reported because of the great difficulty of forming abundant porous microstructures on hard metals. To date, it has still been a substantial challenge to create slippery porous microstructures on medical metal materials and then improve the hemocompatibility of those implantable materials.

NiTi alloys are an ideal bioengineering material that is widely used as the interventional medical scaffold in the modern medical field because of their excellent shape memory property, superelasticity, and biocompatibility.[18–20] In this paper, we reported a novel strategy to prepare a SLIPS on a NiTi alloy substrate. The common Gaussian laser beam was changed to a cone-shaped Bessel beam which directly induced the formation of a deep porous microstructure on the surface of the NiTi alloy. As the porous NiTi alloy was further stored in air to lower the surface energy and infused with a lubricant, the SLIPS was successfully fabricated and effectively repelled water and blood. The adhesion of fibrinogen and bacteria, the coagulation property, and the antibacterial property of the SLIPS were investigated in comparison with those of the untreated NiTi alloy. It was demonstrated that the hemocompatibility of the NiTi alloy substrate was greatly improved by the laser-induced SLIPS.

2. Results and discussion

2.1 Preparation of the porous microstructure

The porous microstructure plays a crucial role in the formation of the SLIPS.[21–24] The features of an ultrashort pulse width and ultrahigh peak energy allow the femtosecond laser to ablate almost any materials, including hard implantable medical materials.[25–31] In comparison with the general Gaussian laser beam, the Bessel laser beam has a longer depth of the focal field and a smaller focal spot.[32–34] Therefore, the Bessel laser beam is more suitable for preparing deep microhole structures than the Gaussian laser beam.[32] To directly build porous microstructures on the NiTi alloy, we changed the common Gaussian laser beam to the Bessel laser beam and used a femtosecond Bessel laser to process the NiTi alloy. The microfabrication system based on the Bessel laser beam is shown in Fig. 1a. The femtosecond laser pulse trains with high frequency were generated from a fiber laser. The intensity distribution of the original laser beam is in agreement with the traditional Gaussian profile. Through an axicon, the Gaussian distribution was spatially shaped into a Bessel profile, as shown in the inset illustration of Fig. 1a. The core (0 order) of the Bessel profile was ~45.0 μm in diameter. The transversal Bessel profile can be sustained within a cone-shaped three-dimensional (3D) space, and the length of the cone reaches 57.3 mm (for a laser spot of 1 mm in diameter) along the propagation direction. Then, the femtosecond Bessel beam was focused onto the surface of the NiTi alloy by an objective lens. The core diameter of the Bessel beam was compressed to ~1.80 μm after focusing. When a single pulse of the compressed femtosecond Bessel beam irradiated the NiTi alloy, most of the laser energy was absorbed by the free electrons localized on the NiTi alloy surface. The free electrons reached a high energy state on the femtosecond timescale during femtosecond laser excitation. Then, the electrons transferred energy to the local lattice, forming a nonequilibrium state, which occurred in several picoseconds. To maintain the local thermal equilibrium, the energy of high-energy electrons was transferred to the local lattice through electron–phonon coupling. When the temperature of the lattice was higher than the phase explosion temperature, the NiTi alloy underwent strong plasma ejection and formed a porous structure. Meanwhile, the plasma ejection process applied a recoil force to the NiTi alloy and induced the melting material to be squeezed out to form a material splashing and pile-up. A part of the ejected material resolidified and deposited on the surface of the NiTi alloy in the form of nanoparticle aggregation or dispersion. Since the energy of a single pulse is limited, only a small amount of material with a thickness of tens of nanometers was removed from the NiTi alloy surface. With a laser pulse train, a series of laser pulses in a train can irradiate at nearly the same position. Thereby, the NiTi alloy surface can be continuously removed layer by layer, finally resulting in a deep hole generated under the accumulated damage. The combined action of the shaped laser Bessel beam and pulse train has the potential to induce a microporous structure on the surface of the NiTi alloy.

Fig. 1b and e show the simulation results of the NiTi alloy surface treated with a single femtosecond laser pulse train. A crater can be generated by both a Gaussian laser beam and a Bessel laser beam under the same processing parameters. The diameter and the depth of the Gaussian beam-induced crater were 12.4 μm and 14.8 μm, respectively (Fig. 1b). Regarding the Bessel beam, the generated hole had a diameter of 1.8 μm and a depth of 13.3 μm and was surrounded by a ring structure with a diameter of 4.2 μm (Fig. 1e). The formation of the deep microhole and the ring structure corresponded to the 0^{th} order and 1^{st} order energy distribution of the Bessel beam, respectively. The simulation results indicate that the Bessel laser beam-induced microhole had a higher aspect ratio than that processed by the common Gaussian laser.

Fig. 1c and d show the scanning electron microscopy (SEM) images of the NiTi surface after ablation by the Gaussian laser beam. A big crater with a diameter of ~6.5 μm is generated with a smaller and shallow cavity at the bottom. The incident laser was reflected at the entrance of the crater. The incident laser interfered with the reflected laser on the walls of the crater. This interference led to a spatial modulation of the energy density and generated a cavity with a diameter of

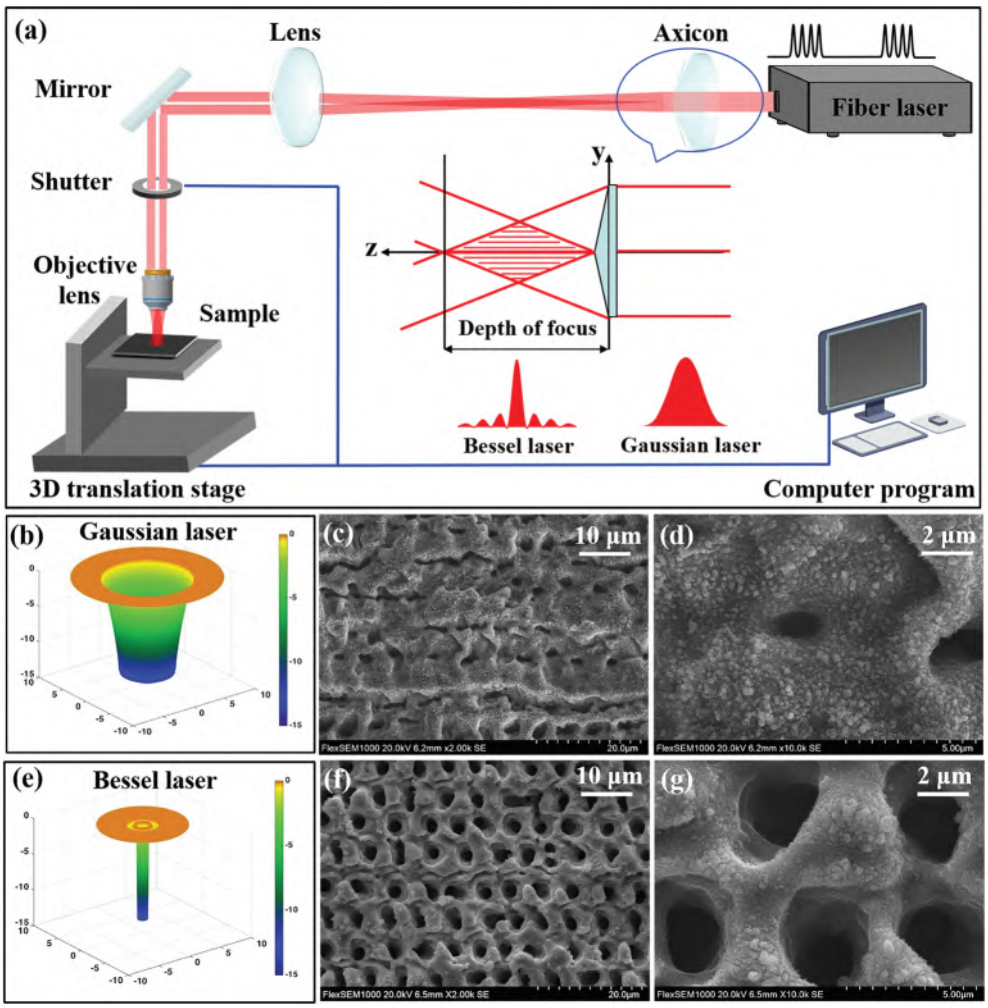

Fig. 1 Fabrication of a porous microstructure on the NiTi alloy by femtosecond laser processing. (a) Microfabrication system based on the femtosecond Bessel laser beam. Inset: Changing the original Gaussian laser beam to the Bessel laser beam through an axicon. (b) Simulation result of the NiTi alloy surface treated with a single pulse train of the femtosecond Gaussian laser. (c and d) Surface morphology of the NiTi alloy after being processed by the femtosecond Gaussian laser. (e) Simulation result of the NiTi alloy surface treated with a single pulse train of the femtosecond Bessel laser. (f and g) Surface morphology of the NiTi alloy after being processed by the femtosecond Bessel laser.

~2 μm where the energy density is strongest in the interior of the crater.[33] Because the distance between adjacent ablation points is smaller than the diameter of the craters, the following laser pulse train is superimposed on the preceding crater. The preceding crater was flattened by the pulse trains of the following to form a shallow crater with a diameter of ~6.5 μm. For the substrate processed by the Bessel laser, abundant pores were created on the NiTi alloy surface (Fig. 1f and g). The diameter of the pores is only 3 μm. Those microholes look very deep, and their bottoms are not visible from the SEM images. The cross-sectional SEM image shows that the depth of the microholes is approximately 30 μm, as shown in Fig. S1 (ESI†). The aspect ratio of the laser-induced microholes is as high as 10. The 3D profile of the structured NiTi alloy confirms that the porous microstructure is very uniform (Fig. S2, ESI†). In comparison with those generated by the Gaussian laser, the microscale pores generated by the Bessel laser are smaller and more uniform. The experimental results are consistent with those of the theoretical analysis. The formation of such micropores with high aspect ratios is ascribed to the features of the femtosecond Bessel laser, *i.e.*, the long depth of the focal field and the small focal spot. Therefore, the femtosecond Bessel laser has a strong capacity to prepare deep micropores with high aspect ratios on metal materials.[34–36]

The energy of the pulse train can be tuned by the number of laser pulses in a single train, which has an important influence on the morphology of the induced porous microstructure, as shown in Fig. 2. When an energy of 534 μJ was applied, only nonuniform and shallow microholes were induced on the NiTi alloy surface (Fig. 2a and b). When the energy of the pulse train increased from 534 μJ to 814 μJ and then to 1085 μJ, the surface proportion of the porous microstructure as well as the depth of the microholes increased because of the accumulation of the ablation process (Fig. 2a–f). When the energy

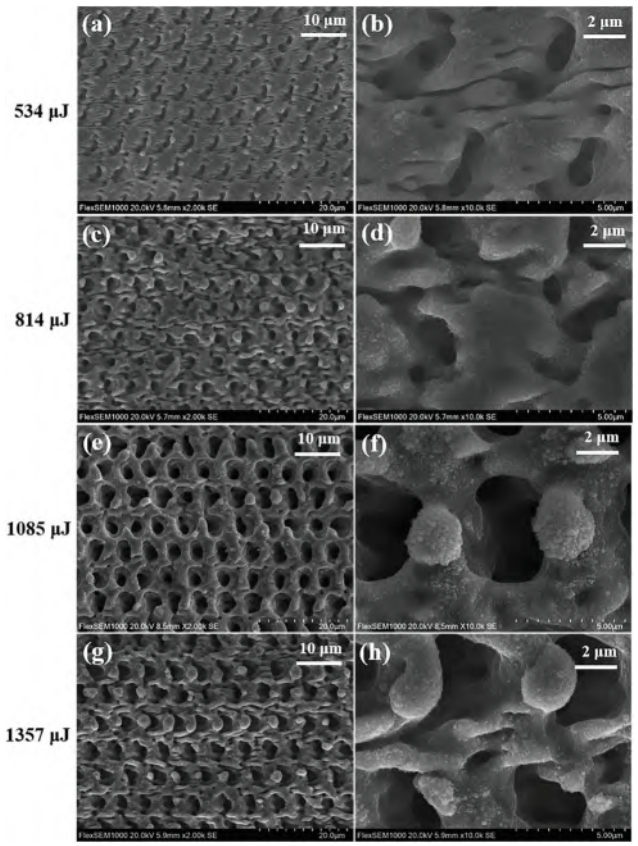

Fig. 2 Morphologies of the NiTi alloy treated with the Bessel laser at different energies of the pulse train. (a and b) 534 μJ, (c and d) 814 μJ, (e and f) 1085 μJ, and (g and h) 1357 μJ.

increased to 1085 μJ, uniform deep micropores formed on the surface of the NiTi alloy and the shape of the holes became close to circular (Fig. 2e and f). As the energy further increased to 1357 μJ, the laser-ablated domains by the adjacent pulse trains began to overlap so that the generated microholes became messy and irregular (Fig. 2g and h). Therefore, the laser-induced porous microstructure prepared at an energy of 1085 μJ, which has uniform and deep pores, was selected as the optimal substrate for fabricating the SLIPS.

2.2 Fabrication of the SLIPS

The preparation of the SLIPS based on the Bessel laser-induced porous microstructure mainly includes three steps: the formation of the porous microstructure by laser processing, the reduction in the surface energy, and the infusion of the lubricant (Fig. 3a). The untreated flat NiTi alloy is hydrophilic. A water droplet on the NiTi alloy substrate had a water contact angle (CA) of 62° (Fig. 3b). When the NiTi alloy was ablated by the femtosecond Bessel laser, a uniform microporous structure was generated on the surface of the NiTi alloy. The resultant rough porous microstructure was able to enhance the hydrophilicity of the NiTi alloy, with the CA decreased to 12° (Fig. 3c). Simple air storage was adopted to lower the surface energy of the laser-induced porous microstructure, because carbon from the atmosphere readily adsorbs to the femtosecond laser-ablated surfaces.[37–40] Compared to the traditional fluoroalkylsilane modification method that is usually used to reduce surface energy, air storage is safer and nontoxic. Fig. 3g shows the X-ray Photoelectron Spectroscopy (XPS) result of the original laser-ablated NiTi alloy. Carbon exists in the form of C=C (284.5 eV) groups, which mainly come from organic pollutants in the air during the laser ablation. After storing the laser-treated sample in air for seven days, the chemistry of the porous NiTi surface obviously changed. As shown in Fig. 3h, the high-resolution spectra for C 1s can be divided into three peaks, referring to C=C (284.5 eV), C–C/C–H (285.3 eV), and C–O–C/C–O (286.7 eV).[39] The XPS analysis demonstrates that the hydrocarbon groups (C=C and C–C/C–H) were grafted onto the porous surface during the air storage, because the laser-ablated NiTi alloy has a great ability to absorb carbon from the atmosphere.[40] The hydrophobic hydrocarbon groups can effectively lower the surface energy of a substrate. Under the combined action of the micro/nanostructure and spontaneous adsorption of hydrocarbons, the porous NiTi alloy switched from hydrophilic to hydrophobic with a CA of 120° (Fig. 3d). Perfluorodecalin, which is nontoxic and extensively used in medicine, was adopted as the lubricant in this experiment. When the lubricant was further dripped onto the porous NiTi alloy, it spontaneously wetted and penetrated into the porous structure under capillary force. The SLIPS was obtained as a uniform lubricating layer formed on the NiTi alloy surface. A water droplet on the as-prepared SLIPS had a CA of 23° (Fig. 3e). As soon as the SLIPS was slightly tilted, the droplet could easily slide down. Fig. 3f shows the sliding process of a water droplet on the as-prepared SLIPS with a tilted angle of 15°. The sliding behavior indicates that the SLIPS has excellent repellency to liquid.

Fig. 4 shows the result of dripping a blood droplet on the NiTi alloy. Regarding the SLIPS, the blood could retain an ellipsoid shape and slide off the SLIPS without leaving any residue (Fig. 4a–c). In contrast, the blood left a noticeable long trail on the untreated NiTi alloy (Fig. 4d–f). Therefore, the SLIPS has the ability to repel blood and can greatly reduce the blood adhesion of the NiTi substrate.[12]

2.3 Anticoagulation property

The coagulation reaction on an implantable material is primarily caused by the adhesion of fibrinogen.[12,40,41] The adhesion of fibrinogen can promote the aggregation and activation of platelets, finally resulting in a clot backbone.[40–43] In this experiment, the adsorption of fluorescein isothiocyanate (FITC)-labeled bovine fibrinogen on different NiTi substrates was investigated with a laser scanning confocal microscope. Fig. 5a shows the fluorescence microscopy image of the bovine fibrinogen on the untreated NiTi alloy. The measured fluorescence density was 0.313 (Fig. 5d). When the porous microstructure was created on the surface of the NiTi alloy, the adsorption of bovine fibrinogen was enhanced (Fig. 5b). The fluorescence density increased to 0.468, meaning that more

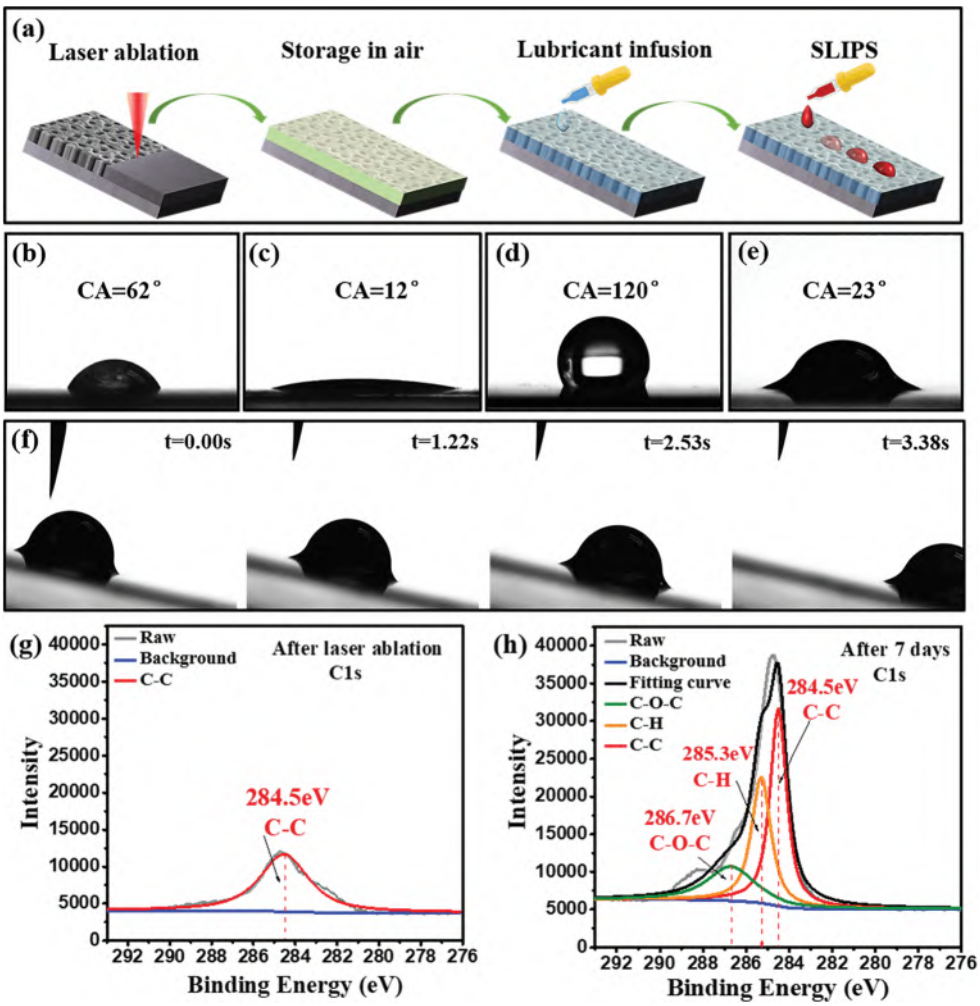

Fig. 3 Fabrication of the SLIPS on a NiTi alloy based on a femtosecond laser-induced porous microstructure. (a) Schematic diagram of the fabrication process. (b–e) Water droplets on different NiTi alloy substrates: (b) the untreated NiTi alloy, (c) the porous surface before storage in air, (d) the porous surface after storage in air for seven days, and (e) the SLIPS. (f) Sliding process of a water droplet on the as-prepared SLIPS with a tilted angle of 15°. (g and h) The XPS analysis of carbon of the porous NiTi alloy (g) before and (h) after storage in air.

bovine fibrinogen adhered to the porous NiTi alloy than on the untreated substrate (Fig. 5d). This is because the contact area between the fibrinogen and NiTi alloy was significantly enlarged by the porous microstructure. Surprisingly, there was almost no bovine fibrinogen adhered to the as-prepared SLIPS (Fig. 5c). The fluorescence density was measured to be only 0.025, which is greatly reduced by 12 times compared to that of the untreated NiTi alloy (Fig. 5d). The quantitative result of protein adhesion on the NiTi alloy surfaces was consistent with the measured fluorescence density, as shown in Fig. 5e. The concentration of adhesive protein was 0.97 mg mL^{-1} on the untreated NiTi alloy and 1.561 mg mL^{-1} on the porous surface. The SLIPS significantly decreases the protein concentration to 0.14 mg mL^{-1}, which was very close to zero. The results demonstrate that the SLIPS can prevent coagulation from occurring on the implantable NiTi alloy; that is, the laser-induced SLIPS has a remarkable anticoagulation property.

2.4 Hemolysis property

Hemolysis rate is an important safety index for implantable medical materials and closely related to the properties of the materials.[44] Materials with a lower hemolysis rate produce less toxic substances. When the common NiTi alloy is implanted into the body, the release of Ni ions will damage red blood cells. The hemolytic reaction usually occurs as the NiTi alloy comes into contact with blood, which will threaten the health of the patient. According to the national standard of China, the hemolysis rate of medical materials must be less than 5%.[44] As shown in Fig. 6, the formation of the SLIPS enables the hemolysis rate on the NiTi alloy to decrease from 4.69% to 1.56%, which is remarkably lower than the 5% of the Chinese national standard and 2.61% of the previously reported anodized NiTi alloy.[45] The effective contact area between the NiTi alloy and blood is greatly reduced by the lubricant layer of the resultant SLIPS. Therefore, the toxic Ni ions underneath the

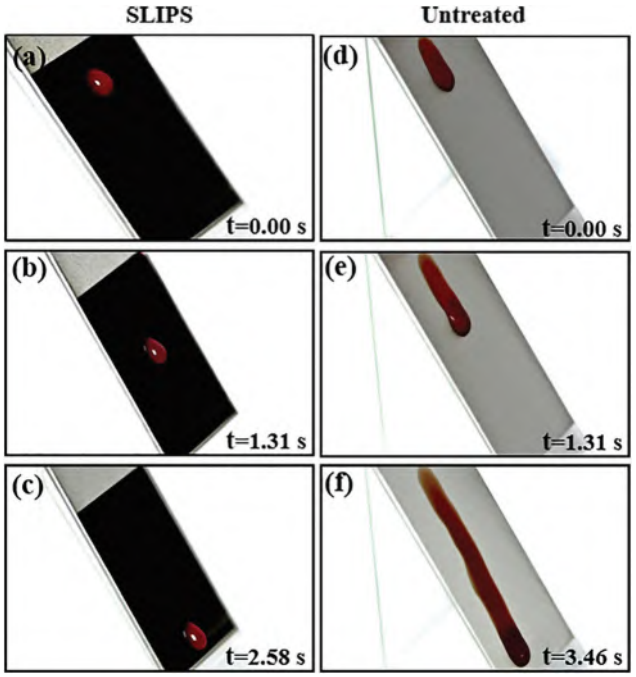

Fig. 4 Dripping a blood droplet on (a, b and c) the SLIPS and (d, e and f) the untreated NiTi alloy. The samples were tilted at 60°.

lubricant layer are prevented from being released and coming into contact with the blood, thus improving the safety of the NiTi alloy.

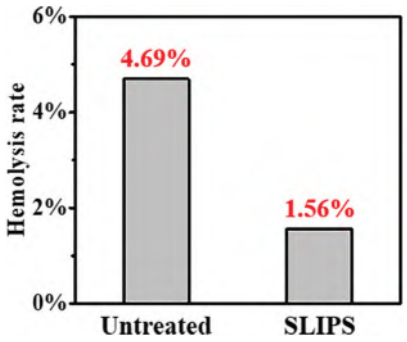

Fig. 6 The hemolysis rate of the untreated alloy and the SLIPS.

2.5 Antibacterial property

Infections caused by bacteria will negatively influence implantable materials.[46–48] Infection can be effectively prevented by reducing bacterial adhesion and biofilm formation.[48] The growth conditions of bacteria on the NiTi alloy were recorded. Two clinical pathogens (*E. coli* and *S. aureus*) were cultured on different substrates. *E. coli* and *S. aureus* are the most common bacteria that cause infections in the medical field.[49] The blank groups of *E. coli* and *S. aureus* were used as the reference, as shown in Fig. 7a and e. Fig. 7b shows the distribution of *E. coli* on the untreated NiTi alloy. Although the total number of bacteria on the untreated NiTi alloy had a slight decrease compared to that on the blank substrate, masses of the bacteria still grew on the NiTi alloy. Only a few *E. coli* bacteria could be

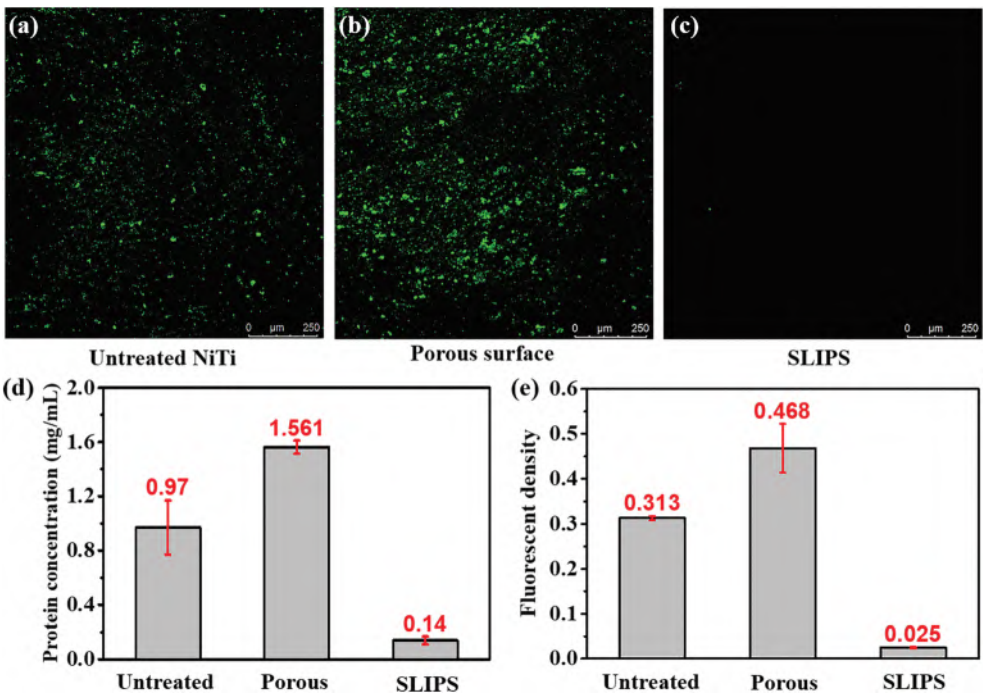

Fig. 5 Fibrinogen adhesion and hemolysis property of the NiTi alloy. (a–c) Fluorescence distribution of the FITC-labeled bovine fibrinogen on (a) the untreated NiTi alloy, (b) the porous NiTi alloy, and (c) the SLIPS. (d) Fluorescence density of the bovine fibrinogen on different NiTi alloy substrates. (e) Protein concentration of the bovine fibrinogen on different NiTi alloy substrates.

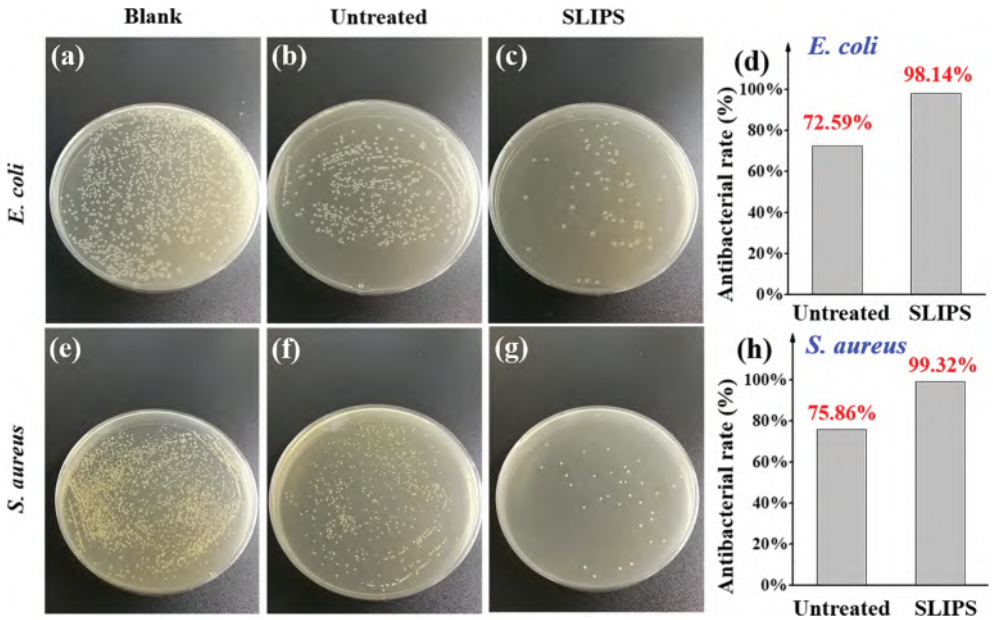

Fig. 7 Growth conditions of bacteria on the NiTi alloy. (a–c) The distribution of *E. coli* on (a) the blank culture substrate, (b) the untreated NiTi alloy, and (c) the as-prepared SLIPS. (d) Antibacterial rate of *E. coli*. (e–g) The distribution of *S. aureus* on (e) the blank culture substrate, (f) the untreated NiTi alloy, and (g) the as-prepared SLIPS. (h) Antibacterial rate of *S. aureus*.

found on the laser-induced SLIPS substrate. The number of *E. coli* on the SLIPS was much smaller than that on the untreated NiTi alloy. In comparison with the blank substrate, the antibacterial rate of *E. coli* increased to 98.14% by the as-prepared SLIPS (Fig. 7d). The growth conditions of *S. aureus* were the same as those of *E. coli* bacteria. As shown in Fig. 7f and g, the cultured *S. aureus* bacteria on the SLIPS were obviously less abundant than on the blank substrate and the untreated NiTi alloy. The formation of the SLIPS led to a 99.32% decrease in *S. aureus* bacteria. The anti-*S. aureus* rate of the SLIPS is 99.32% which is higher than the previously reported 95.6% on the superhydrophobic NiTi alloy surface (Fig. 7h).[50] The results reveal that the growth of more than 98% of bacteria was inhibited on the NiTi alloy after the formation of the SLIPS. Therefore, the as-prepared SLIPS has excellent antibacterial properties.

3. Conclusions

In conclusion, we propose a new method to fabricate a SLIPS on an implantable NiTi alloy based on femtosecond laser processing, which improves the hemocompatibility of the NiTi alloy. A common Gaussian laser beam was changed to a Bessel beam in the processing system. A uniform deep porous microstructure was directly created on the surface of the NiTi alloy. Then, the porous surface was stored in air for seven days to lower the surface energy. After the infusion of perfluorodecalin into the porous microstructure to form a lubricant layer, the SLIPS was successfully fabricated on the NiTi alloy. The as-prepared SLIPS greatly repels water and blood since these liquids can easily slide down the SLIPS. The as-prepared SLIPS is non-toxic because the surface energy of the porous microstructure is lowered by the absorption of hydrocarbon groups from the atmosphere rather than traditional fluoroalkylsilane modification. The adhesion of fibrinogen on the SLIPS is significantly reduced by 12 times compared to that on the untreated NiTi alloy. The formation of the SLIPS decreases the hemolysis rate on the NiTi alloy from 4.69% to 1.56%, which is remarkably lower than the Chinese national standard (5%). In addition, the SLIPS can effectively inhibit the adhesion of bacteria on the NiTi alloy and enhance the bacterial repellency of the NiTi alloy. The antibacterial rates of the resultant SLIPS reach 98.14% and 99.32% for *E. coli* and *S. aureus* bacteria, respectively. The remarkable anticoagulation property, very low hemolysis rate, and antibacterial property demonstrate that the hemocompatibility of the NiTi alloy is greatly improved by the laser-induced SLIPS. We believe that this method can potentially endow various metal implantable substrates with slippery properties and allow implantable medical materials to be applied in a healthier and safer way.

4. Experimental section

4.1 Fabrication of the SLIPS

The schematic diagram of the processing system based on the femtosecond Bessel laser is shown in Fig. 1a. The original femtosecond laser pulses (pulse width = 400 fs; central wavelength = 1030 nm; repetition rate = 2.5 MHz) were generated from a

fiber laser (FemtoYL-40, YSLP). Through the adjustment of the external trigger, the frequency of the output pulse train was 2 kHz, and the frequency of the pulses in every train was 2.5 MHz. The number of the pulses in a single train could be tuned from 125 to 188, 250, and then to 313, corresponding to the train energies of 534 μJ, 814 μJ, 1085 μJ, and 1357 μJ, respectively. Through an axicon (Thorlabs, AX-250, α = 1°), the intensity distribution of the original laser beam was changed from a Gaussian profile to a Bessel profile. The femtosecond Bessel laser was finally focused on the surface of the NiTi alloy (Baoji Seabird metal material Co., Ltd), which was mounted on a moveable platform, by an objective lens (×20, NA = 0.40, Nikon). During the laser processing, the sample surfaces were ablated at a scanning speed of 12 mm s^{-1} and a scanning interval of 6 μm. After laser ablation, the samples were cleaned with acetone, alcohol, and deionized water, in that order. Then, the samples were stored in air for seven days to lower the surface energy. Finally, the lubricant (perfluorodecalin, J&K) was infused into the porous microstructure of the NiTi alloy to form a lubricant layer.

4.2 Characterization

The morphology of the laser-ablated NiTi alloy was observed with a Flex1000 scanning electron microscope (Hitachi, Japan). The 3D profiles of the sample surfaces were measured *via* a LEXT-OLS4000 laser confocal microscope (Olympus, Japan). The contact angle and the sliding angle of 7 μL water droplets on the sample surfaces were measured with a JC2000D contact angle system (Powereach, China). The measured blood is sheep anticoagulant whole blood (5014475, YuduoBio) with a viscosity of 4.373–6.587 mPa s.[51] Elemental analysis was carried out with an X-ray photoelectron spectrometer (AXIS ULtrabld).

4.3 Hemocompatibility test

Fibrinogen adhesion test. The bovine fibrinogen (S12024, Shanghai Yeasen) was dissolved in 0.1 M Na_2CO_3 (Shanghai Sinopharm) solution (PH = 9) to prepare the bovine fibrinogen solution to be crosslinked with a concentration of 2 mg ml^{-1}. Fluorescein isothiocyanate (FITC, S19127, Shanghai Yeasen) was dissolved in an anhydrous DMSO solution (D8371, Solarbio) to prepare the FITC solution with a concentration of 1 mg mL^{-1}. 50 μL of the FITC solution was dripped in 5 μL increments into 1 mL of the bovine fibrinogen solution to form a mixed solution. Then, the mixed solution was incubated for 8 hours at 4 °C in the dark. Finally, 500 μL of the NH_4CL solution (Shanghai Sinopharm, 1 mol L^{-1}) was dripped into the mixed solution. The mixed solution was incubated for 2 hours at 4 °C in the dark to obtain the FITC-labeled bovine fibrinogen. The untreated NiTi alloy, the porous surface, and the SLIPS were put into PBS solutions (P1020, Solarbio) with the FITC-labeled bovine fibrinogen (2 mg mL^{-1}) and incubated for 1 hour at 37 °C. All samples were washed five times with PBS solution to remove the unadhered bovine fibrinogen. The samples were dried by nitrogen. The fibrinogen adhesion on samples was observed with a laser scanning confocal microscope (TCS SP8, Leica). The samples were immersed in aqueous solutions containing 1 wt% SDS (S1010, Solarbio) and shaken for 1 hour to remove the bovine fibrinogen adhered on the surface of the samples. The protein concentration was measured with a BCA protein detection kit (KGPBCA, KeyGEN). A microplate reader (MK3, Thermo) measured the absorbance of the SDS solution containing the bovine fibrinogen at 562 nm. All measurements were repeated three times.

Hemolysis test. The sheep blood (Xi'an Liyang) for the anticoagulation test was diluted with 0.9% NaCl (Tianjin Yili) solution (normal saline) at a ratio of 4 : 5. The untreated NiTi alloy, the porous NiTi alloy, and the SLIPS were put into test tubes. 10 mL of normal saline was dripped into test tubes, and the samples were incubated for 30 minutes at 37 °C. 0.2 mL of the diluted anticoagulated sheep blood was dripped into the test tubes. The test tubes were shaken evenly and cultured for 60 minutes at 37 °C. The solutions in the test tubes were pipetted into centrifugation tubes and centrifuged at 3000 rpm for 5 minutes (Velocity 15 μR, Dynamica). The supernatants of the test tubes were taken out, and the absorbance values at a wavelength of 545 nm were measured with a microplate reader (SpectraMax i3, Molecular Device). All measurements were performed under the same temperature conditions. The positive control group was a mixture of 10 mL of normal saline and 0.2 mL of the diluted anticoagulated sheep blood. The negative control group was a mixture of 10 mL of distilled water and 0.2 mL of the diluted anticoagulated sheep blood. All measurements were repeated three times. The calculation formula for hemolysis rate is

$$\text{hemolysis rate} = \frac{D_t - D_{nc}}{D_{pc} - D_{nc}}$$

D_t, D_{nc}, and D_{pc} are the absorbance of the materials, the absorbance of the negative control group, and the absorbance of the positive control group, respectively.

Antibacterial test. Appropriate *S. aureus* and *E. coli* colonies were selected from a nutrient agar plate. The diameter of each colony was at least 1 mm. Five or more colonies with good growth and similar morphologies were selected for inoculation in the culture medium for 18 hours. The absorbance value of each bacterial solution was measured. *S. aureus* and *E. coli* had absorbance values of 0.875 and 0.789 at a wavelength of 600 nm, respectively. *E. coli* and *S. aureus* were diluted to 1 × 10^6 CFU mL^{-1}. The untreated NiTi alloy and the SLIPS were placed in Petri dishes. 200 μL bacterial solution was dripped onto the samples, and the samples remained at room temperature for 2 hours. The samples were rinsed several times with the sterile PBS solution to remove unadhered bacteria. Then, the sterile physiological saline was dripped into the samples, and the samples were agitated in a vortex oscillator (VORTEX QL-902) for 30 seconds to wash off the bacteria attached to the material. Then, 100 μL of the washing solution was absorbed, and the washing solution was inoculated on a nutrient agar plate for 18 hours. Finally, the number of bacteria on the nutri-

ent agar plate was calculated. All measurements were repeated three times. The calculation formula of the antibacterial rate is

$$\text{antibacterial rate} = \frac{D_b - D_t}{D_b}$$

D_b and D_t are the numbers of bacteria in the blank group and test group, respectively.

4.4 Numerical simulation

To compare the difference of ablation results between the Gaussian laser and the Bessel laser, the theoretical morphologies of the Gaussian laser (Fig. 2a) and the Bessel laser (Fig. 2d) were simulated.[52,53] The thermal deposition inside the NiTi alloy was calculated by resolving a deformed Maxwell equation shown in eqn (1):

$$\frac{d\varepsilon}{dz} = \frac{i}{2k} \cdot \left(\frac{\partial^2}{\partial r^2} + \frac{1}{r} \cdot \frac{\partial}{\partial r}\right)\varepsilon - \frac{\varepsilon}{z_p} \quad (1)$$

In eqn (1), ε is the normalized electric field with the unit of $(2P_{in}/\pi w_0^2)^{0.5}$ and k is the wave vector in NiTi. z_p indicates the energy absorption along the z direction. P_{in} is $E_{in}/(t_p\sqrt{\pi/2})$. t_p is the pulse width, and E_{in} is the pulse energy. w_0 is the diameter of the focused Gaussian beam when the Gaussian beam was applied, and $R_c \cdot w_1$ is the diameter when the Bessel beam was applied; w_1 is the diameter of the beam before the axicon and R_c is the compression ratio for the 4f system shown in Fig. 1a. The pulse energy was deposited into free electrons first and then coupled into phonons based on a simplified two-temperature model (TTM) in eqn (2) and (3):

$$C_e \frac{dT_e}{dt} = g(T_e - T_p) + \frac{\varepsilon^2}{z_p} \quad (2)$$

$$C_p \frac{dT_p}{dt} = g(T_e - T_p) \quad (3)$$

C_e is the electron heat capacity shown as $C_0 \cdot T_e$, in which C_0 is 67.5 J $(m^{-3}\ K^{-2}$. C_p is the phonon heat capacity with a value of 5.36×10^6 J $m^{-3}\ K^{-1}$. g is the electron–phonon parameter with a value of 7.01×10^{18} J $m^{-3}\ K^{-1}\ s^{-1}$. The energy deposition and electron coupling occur on an ultrafast time scale during which the thermal expansion of both electrons and phonons can be ignored. The position where the phonon temperature, T_p, reaches the boiling temperature was defined as immediate vaporization to simplify the model. The remaining part of the NiTi alloy appeared in the next iteration to acquire the electric field and thermal deposition of the next pulse. The iteration time was defined as the pulse number.

Conflicts of interest

There are no conflicts to declare.

Acknowledgements

This work was supported by the National Natural Science Foundation of China under grant no. 61875158, 61435005, and 61805192, the National Key Research and Development Program of China under grant no. 2017YFB1104700, and the Fundamental Research Funds for the Central Universities.

References

1 A. Chauhan, A. Bernardin, W. Mussard, I. Kriegel, M. Esteve, J. M. Ghigo, C. Beloin and V. Semetey, *J. Infect. Dis.*, 2014, **210**, 1347.
2 N. Huang, P. Yang, Y. X. Leng, J. Y. Chen, H. Sun, J. Wang, G. J. Wang, P. D. Ding, T. F. Xi and Y. Leng, *Biomaterials*, 2003, **24**, 2177.
3 G. Chen and Q. Wu, *Biomaterials*, 2005, **26**, 6565.
4 D. Wu, X. Chen, T. Chen, C. Ding, W. Wu and J. Li, *Sci. Rep.*, 2015, **5**, 11105.
5 A. K. Epstein, T. S. Wong, R. A. Belisle, E. M. Boggs and J. Aizenberg, *Proc. Natl. Acad. Sci. U. S. A.*, 2012, **109**, 13182.
6 X. Cao, J. Zhang and D. Y. Geng, *J. Thromb. Haemostasis*, 2019, **48**, 68.
7 A. Patrignani, G. Palmieri, N. Ciampani, V. Moretti, A. Mariani and L. Racca, *G. Ital. di Cardiol.*, 2018, **19**, 54.
8 T. S. Wong, S. H. Kang, S. K. Y. Tang, E. J. Smythe, B. D. Hatton, A. Grinthal and J. Aizenberg, *Nature*, 2011, **477**, 443.
9 W. Q. He, P. Liu, J. Q. Zhang and X. Yao, *Chem. – Eur. J.*, 2018, **24**, 14864.
10 J. M. Nokes, R. Liedert, M. Y. Kim, A. Siddiqui, M. Chu, E. K. Lee and M. Khine, *Adv. Healthcare Mater.*, 2016, **5**, 593.
11 H. Wu, Y. Jiao, C. Zhang, C. Chen, L. Yang, J. Li, J. Ni, Y. Zhang, C. Li, Y. Zhang, S. Jiang, S. Zhu, Y. Hu, D. Wu and J. Chu, *Nanoscale*, 2019, **11**, 4803.
12 D. C. Leslie, A. Waterhouse, J. B. Berthet, T. M. Valentin, A. L. Watters, A. Jain, P. Kim, B. D. Hatton, A. Nedder, K. Donovan, E. H. Super, C. Howell, C. P. Johnson, T. L. Vu, D. E. Bolgen, S. Rifai, A. R. Hansen, M. Aizenberg, M. Super, J. Aizenberg and D. E. Ingber, *Nat. Biotechnol.*, 2014, **32**, 1134.
13 M. Tenjimbayashi, J. Y. Park, J. Muto, Y. Kobayashi, R. Yoshikawa, Y. Monnai and S. Shiratori, *ACS Biomater. Sci. Eng.*, 2018, **4**, 1871.
14 K. Doll, I. Yang, E. Fadeeva, N. Kommerein, S. P. Szafranski, G. B. D. Wieden, A. Greuling, A. Winkel, B. N. Chichkov, N. S. Stumpp and M. Stiesch, *ACS Appl. Mater. Interfaces*, 2019, **11**, 23026.
15 S. Yuan, S. Luan, S. Yan, H. Shi and J. Yin, *ACS Appl. Mater. Interfaces*, 2015, **7**, 19466.
16 C. Howell, A. Grinthal, S. Sunny, M. Aizenberg and J. Aizenberg, *Adv. Mater.*, 2018, **30**, 1802724.
17 M. Badv, S. M. Imani, J. I. Weitz and T. F. Didar, *ACS Nano*, 2018, **12**, 10890.

18 Y. Chun, D. S. Levi, K. P. Mohanchandra and G. P. Carman, *Mater. Sci. Eng., C*, 2009, **29**, 2436.
19 L. Sun, W. M. Huang, Z. Ding, Y. Zhao, C. C. Wang, H. Purnawali and C. Tang, *Mater. Des.*, 2012, **33**, 577.
20 M. Mehrpouya, A. Gisario, A. Rahimzadeh, M. Nematollahi, K. S. Baghbaderani and M. Elahinia, *Int. J. Adv. Manuf. Tech.*, 2019, **105**, 4691.
21 Y. Zhang, Y. Jiao, C. Chen, S. Zhu, C. Li, J. Li, Y. Hu, D. Wu and J. Chu, *Langmuir*, 2019, **35**, 10625.
22 T. F. Xiang, M. Zhang, H. R. Sadig, Z. C. Li, M. X. Zhang, C. D. Dong, L. Yang, W. M. Chan and C. Li, *Chem. Eng. J.*, 2018, **345**, 147.
23 U. Manna and D. M. Lynn, *Adv. Mater.*, 2015, **27**, 3007.
24 S. Sett, X. Yan, G. Barac, L. W. Bolton and N. Miljkovic, *ACS Appl. Mater. Interfaces*, 2017, **9**, 36400.
25 J. Yong, C. Zhang, X. Bai, J. Zhang, Q. Yang, X. Hou and F. Chen, *J. Colloid Interface Sci.*, 2021, **582**, 1203.
26 J. Song, F. Guan, W. Pan, Z. Liu, J. Sun, S. Ling, X. Deng and Y. Sun, *Adv. Funct. Mater.*, 2020, 1910778.
27 J. L. Yong, C. Zhang, X. Bai, J. Zhang, Q. Yang, X. Hou and F. Chen, *Adv. Mater. Interfaces*, 2020, **7**, 1901931.
28 J. Song, L. Huang, C. Zhao, S. Wu, H. Liu, Y. Lu, X. Deng, C. J. Carmalt, I. P. Parkin and Y. Sun, *ACS Appl. Mater. Interfaces*, 2019, **11**, 45345.
29 J. L. Yong, F. Chen, Q. Yang, D. S. Zhang, G. Q. Du, J. H. Si, F. Yun and X. Hou, *J. Phys. Chem. C*, 2013, **117**, 24907.
30 J. Song, Z. Liu, X. Wang, H. Liu, Y. Lu, X. Deng, C. J. Carmalt and I. P. Parkin, *J. Mater. Chem. A*, 2019, **7**, 13567.
31 H. Ma, M. Cao, C. Zhang, Z. Bei, K. Li, C. Yu and L. Jiang, *Adv. Funct. Mater.*, 2018, **28**, 1705091.
32 R. Stoian, M. K. Bhuyan, G. D. Zhang, G. H. Cheng, R. Meyer and F. Courvoisier, *Adv. Opt. Technol.*, 2018, **7**, 165.
33 J. Aldana, C. Mendez, L. Roso and P. Moreno, *J. Phys. D: Appl. Phys.*, 2005, **38**, 2764.
34 Q. Xie, X. W. Li, X. L. Jiang, B. Xia, X. L. Yan, W. W. Zhao and Y. F. Lu, *Appl. Phys. A*, 2016, **122**, 136.
35 Z. Yao, L. Jiang, X. Li, A. Wang, Z. Wang, M. Li and Y. Lu, *Opt. Express*, 2018, **26**, 21960.
36 Y. Matsuoka and M. Kohno, *Rev. Laser Eng.*, 2004, **32**, 348.
37 A. Y. Vorobyev and C. Guo, *J. Appl. Phys.*, 2015, **117**, 033103.
38 A. M. Kietzig, S. G. Hatzikiriakos and P. Englezos, *Langmuir*, 2009, **25**, 4821.
39 L. Shen, M. Xu, W. Jiang, M. Qiu, M. Fan, G. Ji and Z. Tian, *Appl. Surf. Sci.*, 2019, **489**, 25.
40 P. Liu, L. Cao, W. Zhao, Y. Xia, W. Huang and Z. Li, *Appl. Surf. Sci.*, 2015, **324**, 576.
41 A. Fouras, S. P. Jackson, E. Westein, E. Tolouei, W. S. Nesbitt, J. Fu, J. Carberry, F. J. Tovar-Lopez and A. Mitchell, *Nat. Med.*, 2009, **15**, 665.
42 R. J. Daniello, N. E. Waterhouse and J. P. Rothstein, *Phys. Fluids*, 2009, **21**, 85103.
43 S. Moradi, N. Hadjesfandiari, S. F. Toosi, J. N. Kizhakkedathu and S. G. Hatzikiriakos, *ACS Appl. Mater. Interfaces*, 2016, **8**, 17631–17641.
44 Q. Wang, L. Tan and K. Yang, *J. Mater. Sci. Technol.*, 2015, **31**, 845.
45 C. L. Chu, R. M. Wang, T. Hu, L. H. Yin, Y. P. Pu, P. H. Lin, Y. S. Dong, C. Guo, C. Y. Chung, K. W. K. Yeung and P. K. Chu, *J. Mater. Sci.: Mater. Med.*, 2009, **20**, 223.
46 K. Doll, E. Fadeeva, J. Schaeske, T. Ehmke, A. Winkel, A. Heisterkamp, B. N. Chichkov, M. Stiesch and N. S. Stumpp, *ACS Appl. Mater. Interfaces*, 2017, **9**, 9359.
47 A. Cunha, A. Elie, L. Plawinski, A. P. Serro, A. M. B. d. Rego, A. Almeida, M. C. Urdaci, M. Durrieu and R. Vilar, *Appl. Surf. Sci.*, 2016, **360**, 485.
48 K. G. Neoh, M. Li, E. Kang, E. Chiong and P. A. Tambyah, *J. Mater. Chem. B*, 2017, **5**, 2045.
49 K. B. Laupland, D. B. Gregson, D. L. Church, T. Ross and J. D. D. Pitout, *Clin. Microbiol. Infect.*, 2008, **14**, 1041.
50 Y. Ma, L. Jiang, J. Hu, H. Liu, S. Wang, P. Zuo, P. Ji, L. Qu and T. Cui, *ACS Appl. Mater. Interfaces*, 2020, **12**, 17155.
51 U. Windberger, A. Bartholovitsch, R. Plasenzotti, K. J. Korak and G. Heinze, *Exp. Physiol.*, 2003, **3**, 431.
52 H. Wang, F. Pöhl, K. Yan, P. Decker, E. L. Gurevich and A. Ostendorf, *Appl. Surf. Sci.*, 2019, **471**, 869.
53 G. Du, Q. Yang, F. Chen, Y. Wu, Y. Ou, Y. Lu and X. Hou, *Int. J. Heat Mass Transfer*, 2015, **87**, 341.